

RESEARCH ARTICLE | JULY 01 2024

The redesigned neutron imaging facility, NORMA at BNC, Budapest



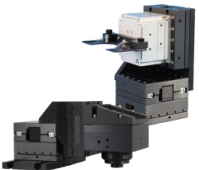
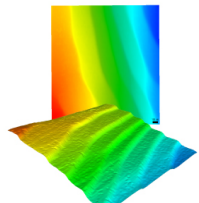
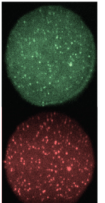
Zoltán Kis  



Rev. Sci. Instrum. 95, 073702 (2024)

<https://doi.org/10.1063/5.0208844>



 MAD CITY LABS INC. www.madcitylabs.com	Nanopositioning Systems 	Modular Motion Control 	AFM and NSOM Instruments 	Single Molecule Microscopes 
---	---	---	--	---

The redesigned neutron imaging facility, NORMA at BNC, Budapest

Cite as: Rev. Sci. Instrum. 95, 073702 (2024); doi: 10.1063/5.0208844

Submitted: 17 March 2024 • Accepted: 7 June 2024 •

Published Online: 1 July 2024



View Online



Export Citation



CrossMark

Zoltán Kis^{a)} 

AFFILIATIONS

Nuclear Analysis and Radiography Department, HUN-REN Centre for Energy Research, Hungarian Research Network, Konkoly-Thege Miklós út 29-33, H-1121 Budapest, Hungary

^{a)} Author to whom correspondence should be addressed: kis.zoltan@ek.hun-ren.hu

ABSTRACT

The Budapest Neutron Center operates the cold neutron beam imaging station, Neutron Optics and Radiography for Material Analysis (NORMA), for non-destructive testing. For the NORMA station, there have been increasing requests to reach higher spatial resolution and the ability to follow time-dependent processes. Therefore, the system used successfully so far was completely redesigned and installed for a variety of tasks. The new system is based on the principle of three independent modules, allowing for highly configurable settings. It is to find the right balance between the necessary spatial resolution, a sufficiently shorter or longer temporal resolution, and a large enough field of view. The systematic study of the setups clearly shows the parameters' effects, helping to make the right choice for the measurement tasks. Among the rarely investigated parameters, we studied both the effect of the pixel binning and the change in the lens f-stop value on the spatial resolution. The newly improved NORMA facility allows the acquisition of high-quality neutron images for planned observations, e.g., local water kinetics in fuel cells.

Published under an exclusive license by AIP Publishing. <https://doi.org/10.1063/5.0208844>

I. INTRODUCTION

The Budapest Neutron Center operates several neutron measurement stations. Imaging is one of the non-destructive testing types available. One of the two imaging facilities is NORMA (Neutron Optics and Radiography for Material Analysis), which uses cold neutrons and is designed to perform neutron imaging of smaller objects (a few centimeters). This facility is located at the end of a neutron guide, away from the reactor's cold neutron source. The very first instrument, which was only temporary at the time, was implemented in 2006 as part of the EU Ancient Charm project.¹ Its unique feature was the possibility to perform position-sensitive elemental analyses [prompt gamma activation analysis, PGAA driven by neutron radiography (NR), neutron tomography (NT)] guided by image information (neutron radiography, tomography, NR, NT). Already then, the increased demand from users was apparent, and by 2012–2015, a redesigned and now permanently operational measuring station was installed.² This facility is an integral part of the NIPS (Neutron-Induced Prompt Gamma-ray Spectroscopy)-NORMA measurement station that has been operational since then. The types of studies conducted cover a wide range

of subjects, from materials science^{3,4} to cultural heritage,^{5–8} from paleontology⁹ to the study of porous materials.^{10,11} Of particular interest are the method's developments, e.g., for PGAA analysis corrected by Monte Carlo simulations^{12,13} or for quality assurance¹⁴ or scintillator development¹⁵ in neutron imaging.

The NIPS detector system, which performs PGAA elemental analysis measurements, has been operating as a leading world-class facility and continues to meet the needs raised. In recent years, however, there have been increasing requests for imaging with considerably higher spatial resolution and the ability to follow time-dependent processes. Among these needs, some of the most important problems are related to energy production and storage. In this field, higher spatial resolution (some tens of microns or better) and variable exposure times (from tenths of a second up to a few times in tens of seconds) are needed to probe the structure and operational characteristics of fuel cells^{16–18} and electric batteries.^{19,20} In contrast, for imaging-driven PGAA measurements, a poorer spatial resolution with shorter exposure times to avoid unnecessary activation is sufficient.^{13,21} In both cases, it is most important to maintain the field of view as large as possible, using spatial and temporal resolution (i.e., exposure times) appropriate to the task at hand.

These conditions together represent conflicting requirements, and it is, therefore, essential to optimize the system parameters. Both our own and international experiences have shown that the requirements cannot be well met by one type of system, and therefore, a system optimized for two sets of tasks was designed at the conceptual design level. In the neutron imaging community, there are beamlines, which serve as good examples of how to design and implement such versatile facilities.^{22–25} In this paper, we present the steps of the recent development of the NORMA imaging system, from design to implementation.

II. METHODS

A. The measuring environment

The cold neutrons are guided from the cold neutron source of the tank-type Budapest Research Reactor operating with a thermal power of 10 MW. The NIPS-NORMA facility is situated at the end of beamline No. 10/1, around 35 m from the reactor core [Fig. 1(a)]. The guide system uses supermirror guides ($m = 2$) for effective neutron transport. It is curved into an S-shape to avoid disturbing background gamma and neutron radiation from the direct line of sight into the reactor core. There are neutron scattering measurement stations upstream of the beam, which decrease the available neutron flux at given neutron wavelengths [e.g., around 4 Å, Fig. 1(b)]. At the end of the rectangular shaped guide ($H \times V = 25 \times 100 \text{ mm}^2$), the beam is permanently divided into an upper and a lower part applying a Li-6 enriched poly sheet with a neutron attenuation factor of at least 1000, and the lower part operates the NIPS-NORMA facility. In this lower beam, a motorized pinhole exchanger and a graphite scatterer are installed, which can adjust the L/D ratio, a measure of the neutron beam's divergence, while at the same time making the beam spot more homogeneous. The pinhole system is fabricated from the above-mentioned type of Li-6 enriched poly sheet. It has three positions with aperture sizes of

550 mm² ($25 \times 22 \text{ mm}^2$, the original), 121.54 mm² ($\varnothing 12.44 \text{ mm}$), and 9.95 mm² ($\varnothing 3.54 \text{ mm}$). There are two pyrolytic graphite scatterers with 2 and 3 mm thicknesses placed upstream, which could be positioned independently of the pinholes. Graphite is used as a diffuse scatterer that can help smear out, at least partly, the non-uniformity of the beam's intensity distribution and the appearing darker stripes.²⁴ The beam arrives through a flight tube into the sample chamber, with a center situated 260 cm downstream from the guide end. There is an adjustable rectangular beam limiter available at the chamber's inlet to tailor the beam's necessary cross section. The largest cross-sectional area of the neutron beam is c. $43 \times 43 \text{ mm}^2$, the maximum thermal equivalent flux at the center of the beam is $2.7 \times 10^7 \text{ cm}^{-2} \text{ s}^{-1}$, and the spatial distribution of the beam's intensity is inhomogeneous.²

B. Basic conceptual design

One of the main ideas during the conceptual design of the imaging device was to be able to ensure uninterrupted and undistorted elemental analysis measurements when there is no need for imaging. Therefore, the default situation is when none of the imaging system components are in the beamline, but either can be set to a measuring position in a short time if required. With this solution, the structural materials of the imaging equipment do not create an unnecessary gamma radiation background during PGAA measurements.

Furthermore, the basic idea was to build a dual-purpose imaging system. One operates at medium to low spatial resolution (around 100–150 μm on screen), but with sufficiently short temporal resolution (even in real-time mode), if required, with a relatively large field of view. This is, in fact, a more advanced version of the previous system² (called the medium-resolution setup). The other system operates with a higher spatial resolution (about 40–50 μm on screen) but with a lower temporal resolution, using a smaller field of view. This is, in fact, a completely new measurement system (called a high-resolution setup).

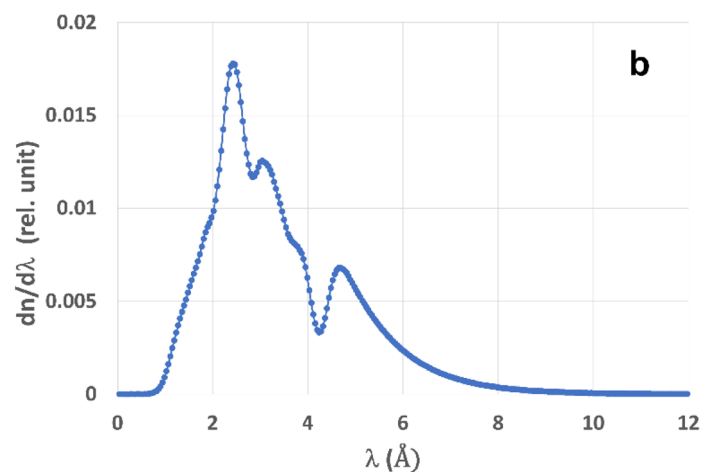
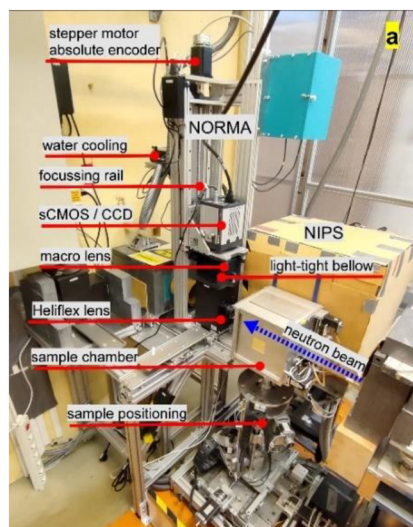


FIG. 1. (a) The overview of the NIPS-NORMA station. (b) The normalized neutron wavelength spectrum of the NORMA station.

C. Detailed design

According to the detailed design, both imaging systems are divided into three main modules. The function of each module follows the established best practices from the last two decades of experience.^{22,23} The modules themselves are a neutron-to-light conversion module, an optical imaging module with a lens, and a digital camera module. The modules are connected to each other in a light-tight manner, which can easily be disconnected and reconnected.

In the neutron-to-light conversion module, a scintillation screen inserted perpendicular to the beam converts the neutron transmission image of the sample into visible light. The NORMA measuring station uses three types of green-light-emitting screens that complement each other quite well. The most commonly used ⁶LiF/ZnS screen has the highest light yield but limited spatial resolution, mainly due to its larger thickness (100 μm) and partly because the charged triton particles can travel relatively far away from the Li(n, α)³H reaction site before they create photons in the ZnS scintillator material.^{26,27} At NORMA, we are gathering experiences using a B-10-based screen, which is at the present time a promising candidate because medium light yield and better spatial resolution are expected compared to that of ⁶LiF/ZnS screens.^{15,28} Among our screens, the Gd-based one has the best spatial resolution because the high neutron capture efficiency of Gd makes it possible to apply a thin (10 μm) scintillation layer, where the charged particle's mean free path from the Gd(n, γ + IC_e-) reaction is shorter compared to that in the LiF-based screens.²⁹ Unfortunately, its light yield is the lowest, which implies the necessity of effective light collection in the optical system. The detailed properties of each screen are given in Table I. Although the screens mounted might be the

same, the conversion module unit is fundamentally different for the medium- and high-resolution setups. To achieve the best possible light gathering in the optical imaging module, a macro lens³⁰ with high brightness (i.e., a lower f-stop value) is used in each setup (see Table I). This fixed focal length prime lens has negligible geometric distortions. In a medium-resolution setup, the lens works by focusing on its closest focus distance, while in a high-resolution setup, it focuses on infinity as a member of an infinity corrected tandem system.²² The digital camera module can currently host three different cameras: a CDD (Charge-Coupled Device, operating since 2012) and two sCMOS ones (scientific Complementary Metal–Oxide–Semiconductor, recently bought). The pixel size and the size of the camera chip vary in a wide range to be able to find the best combination for a given task (see Table I). The CCD (Andor iKon-M 934) and one of the sCMOS cameras (QHY 600M PRO) are better used for measurements with longer exposure times, while for faster exposures, the Andor Neo 5.5 sCMOS camera is used more frequently.

D. Medium-resolution setup

In the medium-resolution setup [Fig. 2(a)], scintillation screens with a 50 × 50 mm² size can interchangeably be mounted on a protruding nose. A 45° mirror is mounted in the beam path behind the screen, which reflects the light onto the optical imaging module using a lens perpendicular to the beam. The nose's length is twice the length of the scintillation screen, to exclude double or multiple reflections from the mirror and the screen into the camera. The nose, moreover, can also be pushed into the shielded sample chamber to reach a minimal distance between the sample and the screen

TABLE I. Functional units of the NORMA measurement system and their characteristics.

Functional unit	Characteristics
Scintillator screen (all from RC Tritec Ltd., Switzerland)	<ul style="list-style-type: none">• Li100: 100 μm thick ⁶Li/ZnS:Cu (1/2), green: 520 nm, subst.: 1.5 mm Al• B50: 50 μm thick ¹⁰B₂O₃/ZnS:Cu (1/2), green: 540 nm, subst.: 1 mm Al• Gd10: 10 μm thick Gd₂O₂S:Tb, green: 447/549 nm, subst.: 1.5 mm Al
Light-tight house	<ul style="list-style-type: none">• Medium-resolution setup:<ul style="list-style-type: none">◦ Al coated quartz mirror (3 mm thick) set at 45° to the beam• High-resolution setup:<ul style="list-style-type: none">◦ XR-Heliflex lens with focal length = 122 mm (f-stop = 2.6, NA = 0.2)◦ it is the objective (collimator) lens in the tandem setup
Lens	<ul style="list-style-type: none">• ZEISS Milvus 2/100M ZF.2 (Nikon)³¹<ul style="list-style-type: none">◦ on closest focus (440 mm): Focal length = 106.8 mm, M = 1:2◦ on infinity focus (tandem setup): Focal length = 97.5 mm◦ it is the imaging (recording) lens in the tandem setup
Standard imaging detector	<ul style="list-style-type: none">• Back-illuminated Andor iKon-M 934 CCD camera with 1024 × 1024 pixels and 16-bit pixel depth, pixel size: 13 μm• Front-illuminated Andor Neo 5.5 sCMOS camera with 2560 × 2160 pixels and 16-bit pixel depth, pixel size: 6.5 μm• Back-illuminated QHY 600M PRO BSI liquid cooled sCMOS camera with 9600 × 6422 pixels and 16-bit pixel depth, pixel size: 3.76 μm

06 July 2024 13:57:13

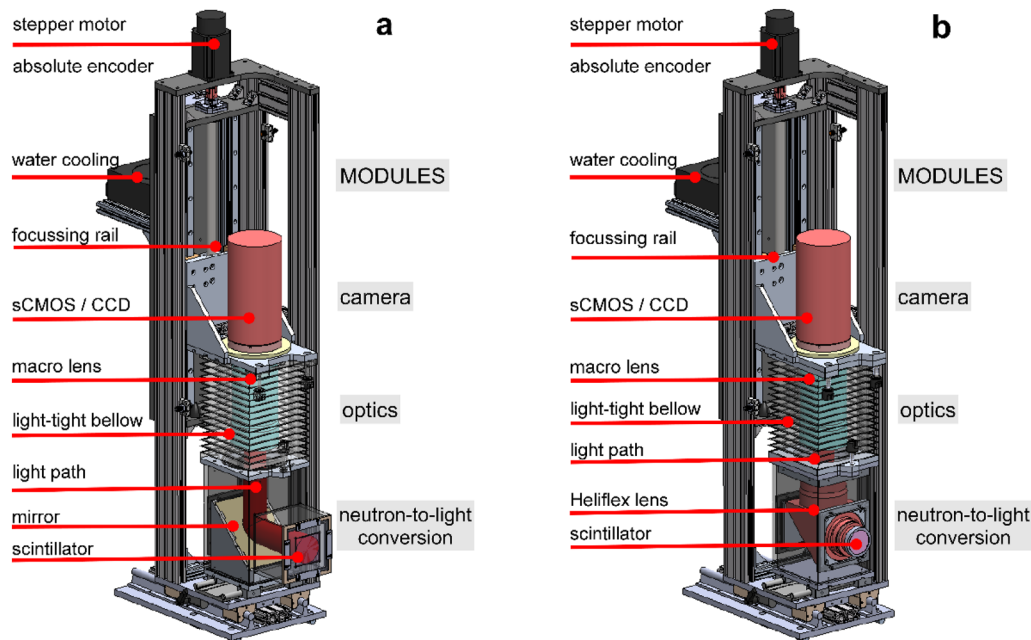


FIG. 2. Conceptual and functional structure of two main setups at NORMA: (a) medium-res. and (b) high-res.

when, e.g., image-driven PGAA is carried out. The short object-to-screen distance is advantageous to reach a better spatial resolution by minimizing the geometrical blur from the diverging beam. The front surface of the 3 mm thick flat quartz mirror is Al-coated to ensure a proper light path. This type of coating, together with the low level of impurities in the mirror's material,³² prevents longer-term activation, too.

In the medium-resolution setup, the macro lens is focused to its closest focus at 440 mm, and this focal plane is then set to the plane of the scintillation screen. In this case, the actual focal length increases to 106.8 mm, the f-stop value changes from 2 to 3.6, and the magnification of the system is $M = 0.5$. If necessary, using a macro distance ring between the camera and the lens allows you to set a shorter focal length to increase magnification, but with a loss of brightness. To reach this focused position, the imaging module coupled to the camera module is moved along a 200 mm long vertical rail system with a precision of 2 μm . The movement is driven by a stepper motor, and an absolute encoder records the necessary motor steps.

E. High-resolution setup

In the high-resolution setup [Fig. 2(b)], we use the Gd-based screen because it has the lowest inherent blur. The 10 μm -thick Gadox scintillation screen is mounted at the precise focal plane of an XR-Heliflex collimator lens.³³ This lens is the objective lens in a tandem system, collecting the light from a wide solid angle ($NA = 0.2$, $f_o = 122$ mm). The effectively captured light is then formed into a parallel light image, which is the input image for an imaging lens focused on infinity, creating a so-called infinity corrected optical setup. The imaging lens mounted in the optical imaging module is the Zeiss macro lens. In this case, its focal

length decreases to $f_i = 97.5$ mm while keeping the nominal f-stop value of 2. In this tandem setup,³⁴ the effective focal length is $f_{\text{eff}} = (f_o \times f_i) / (f_o + f_i) = 54.19$ mm, with an effective f-stop value of 1.15, and the magnification of the system (M_t) is the ratio between the focal length of the imaging and objective lens, i.e., $M_t = f_i / f_o = 0.80$.

Tandem systems have advantages when the effective collection of emerging light is critical. To reach a higher spatial resolution in neutron imaging, usually higher collimation of the beam (i.e., a larger L/D ratio) and a smaller effective pixel size (i.e., the size of an area seen by a native camera pixel through the optical system) for higher magnification and a better absorbing but thinner scintillator screen are needed.^{22,23} All these factors point toward an exceptionally low photon flux to be acquired.

F. Spatial resolution evaluation

The spatial resolution of an image is measured by the slanted-edge method, which finds the spatial frequency value for which the Modulation Transfer Function (MTF) falls to 0.1.²² We use a slightly modified version of the Slanted Edge MTF imageJ-FIJI plugin,³⁵ which can work in batch mode for a stack of images. The MTF as a function of the spatial frequencies is analyzed in a user-defined rectangular region of interest (ROI) in an image of a Gd knife-edge (a 25 μm thick and freshly cut Gd stripe mounted on the Al support of the screen), as shown in Fig. 3.

In evaluating the spatial resolution for the medium-resolution setup, the first step is pre-focusing with an optical target, for which a grid pattern is set to the position of the scintillator screen. After having evaluated the stacked images acquired at regularly spaced camera positions, the optimal one is where the sharpest image was taken. In

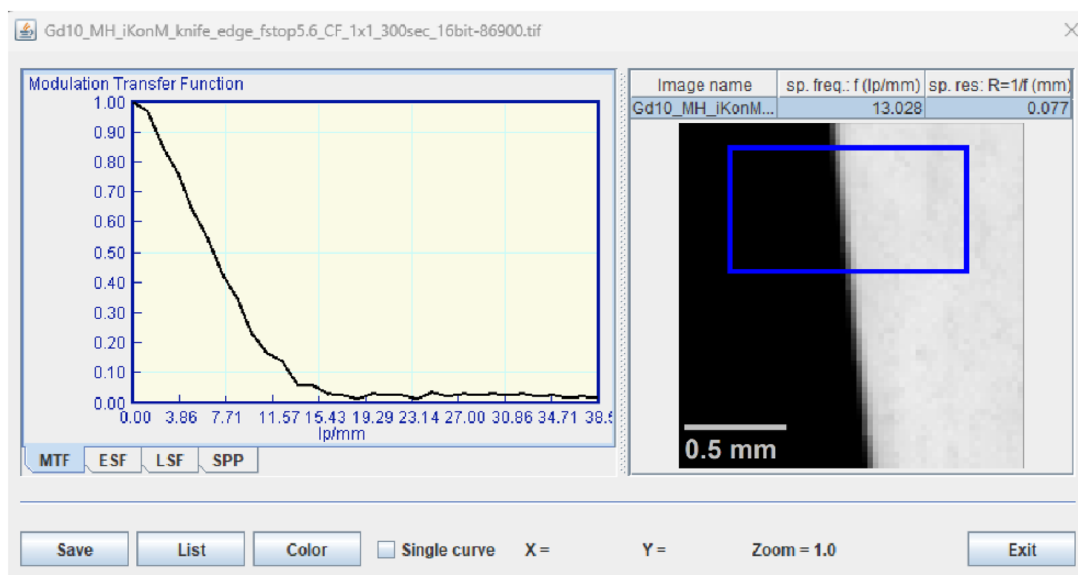


FIG. 3. Result of the MTF plugin: exemplary spatial resolution measurements by slanted Gd knife-edge (Gd10 screen + Milvus100 + iKon-M camera configuration).

the next step, the optical target is changed to the scintillation screen, and the fine-tuning of the focusing is carried out by acquiring neutron radiography images about the Gd knife-edge at regularly spaced camera positions. The f-stop is set to its lowest nominal value (i.e., to 2) because the depth-of-field is the shortest in this case. In the high-resolution setup, the plane of the Gd-based scintillation layer is set to the XR-Heliflex focal plane. This focal plane matches the plane of an XR-Heliflex flange, and the screen is mounted on it with extreme care using a threaded support ring. During the fine focusing of the imaging lens around infinity, a stack of neutron radiography images is acquired about the Gd stripe. We used the slanted edge plugin to find that focus setting, which refers to the highest spatial frequency. Before using the plugin, the outlier removal tool of FIJI was applied to facilitate the slanted edge method. The number of rows in a rectangular ROI was in the order of a few tens to smooth the MTF curve.

The on-screen spatial resolutions were compared in possible screen-camera configurations, on the one hand, to the theoretically calculated best resolutions and, on the other hand, to the spatial resolutions measured by visible light. First, the best theoretical spatial resolutions were calculated based on the Nyquist sampling theorem. In practice, it says the resolution cannot be better than twice the sampling size, i.e., in our case, it is twice the effective pixel size of the actual setup. Second, the measurements using visible light are important because the inherent blur of the scintillation screens does not play a role, and therefore, we can assess this effect separately when imaging is done with screens in the final tests. We conducted several tests with visible light to measure the systems' optical capabilities without the scintillation screens. The light was a normal ambient room light instead of the green one, for which the quantum efficiency of the camera chips is optimized. During the spatial resolution measurements, the lens aperture (i.e., f-stop value) was changed in a wide range (from 2 to 5.6, meaning the amount of light

decreased to 1/8 of its maximum value) to assess effects. The use of scintillation screens will further reduce these spatial resolutions because of their inherent blur.

C. Exposure times

In addition to the spatial resolution, the exposure time required to fill the pixels' well depth also plays a significant role in the measurements as an important factor in the dynamic range that can be achieved. Depending on the type of scintillator material, a large number of photons are emitted by the screen per single detected neutron,^{26,36,37} and multiple photons are detected per neutron. It could happen that these photons saturate the camera for a small number of detected neutrons, thus, resulting in bad neutron statistics. Using a smaller iris aperture in the lens (f-stop) reduces the number of detected photons per neutron and, thus, requires more detected neutrons to saturate the camera, rendering better neutron statistics. From the viewpoint of the sample's neutron activation, we prefer shorter times; however, longer ones tend to provide neutron statistics that are good enough to detect small contrast differences.

The longest exposure time for a given f-stop value is determined by many factors: (a) the rate of cold neutron reactions with the scintillation material (Poisson statistics); (b) the light yield of the scintillation screens; (c) the quantum efficiency of the camera pixels; (d) the well depth of the camera pixels; (e) the setting of the gain, i.e., the electron-ADU (analog-to-digital unit) conversion sensitivity of the camera; (e) the readout range of the analog-to-digital converter (ADC); and (f) the binning of the pixels. From these parameters, the gain, the ADC readout range, and the binning could be set by users to result in good neutron statistics per effective pixel of the scintillation screen before the ADC is saturated. In our tests, after having set the 16-bit or 12-bit range for the ADC, the remaining two parameters (i.e., gain and binning) were set to reach a relative uncertainty

of less than 5% in the number of neutron reactions with scintillation screen material in the central part of the beam.

III. RESULTS AND DISCUSSION

A. Medium-resolution setup

The medium-resolution setup with its multiple configuration options, which are adjustable according to users' demand, is the working horse of the NORMA imaging system. Its most important theoretical parameters are calculated and tabulated in Table II.

During the visible light tests, it was found that the optical systems in all configurations work with the best spatial resolution by setting f-stop values between 4 and 8, as shown in Fig. 4. Theoretically, spatial resolution is directly related to the numerical aperture (NA) of the lens, i.e., a higher NA provides better resolution. Increasing the f-value (i.e., closing the aperture) means a lower NA, which results in a lower achievable resolution. In our case, the Milvus 2/100M lens is designed to follow this trend at f-stops above 4. At lower f-stops (i.e., larger apertures), light rays farther from the optical axis are also involved in the imaging process; however, these degrade the image quality, resulting in poorer spatial resolution.

Having compared the theoretical and measured spatial resolution values, we can assess how the optical system itself deteriorates the theoretical values (see Fig. 5). The results are tabulated for the f-stop of 5.6 both as absolute values and percentage changes in Table III. We can conclude that the most significant percentage change (60%) happened to the system with the smallest native pixel size (QHY600M PRO-3.76 μm), while the less notable change (15%) was for the iKon-M with the largest native pixel size (13.5 μm).

The results of the B50 boron screen were left out of evaluations because they showed poor image quality and very low light yield, with similar exposure times compared to those of Gd-based. It means that further developments are still needed for boron-10 based screens, mainly in terms of light yield and an optimized milling process for grains.¹⁵

The results of spatial resolution measurements of the 3×2 configurations using the three cameras and two scintillation screens (Li100 and Gd10) are shown in the panels of Fig. 5, too. It can clearly be seen that the inherent blur of the scintillation screens masks and overrides the different values obtained from the pure optical system. It means that, if necessary, the f-stop values can effectively be adjusted to limit the amount of light reaching the camera chip to improve the neutron statistics in the image pixels. Of course, in low light conditions, the larger apertures are the preferable choices, provided that the camera system is positioned perfectly in the range of

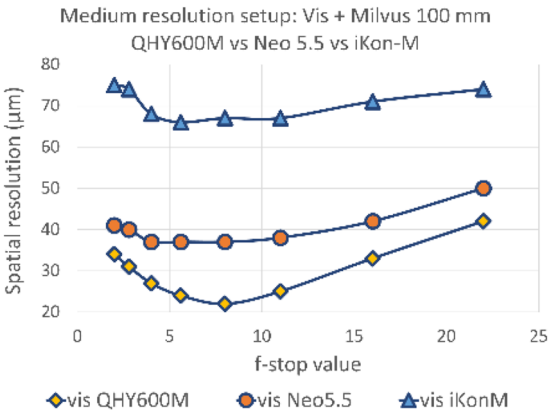


FIG. 4. Measured optical spatial resolution values at different f-stop values with the various camera configurations for the medium resolution setup at the NORMA station.

depth of field to be able to focus on the scintillation screen. Furthermore, the spatial resolution curves clearly show the difference between the various screens, i.e., the Gadox screen has the best resolution, and the LiF/ZnS screen is inferior to it. A detailed comparison is shown in Table III, where one can follow the deterioration effect of a pure optical system and the inherent blurring effect of the scintillation screens in the configurations.

Exposure times for the 16 and 12-bit depth modes without and with binning are shown in Table IV. Here, one can clearly see again the considerable difference between LiF/ZnS and Gd-based screens. In our case, the ratio of measured exposure times, or, in fact, the ratio of light yields, is around the value of 20 calculated from the information provided by the manufacturer. This suggests that the light yields of our screens have not decreased considerably during use. There are ways to shorten the exposure times of the Gd-based screens while keeping the wide dynamic range of 16-bit images. A possibility is to use a camera designed especially for low light environments. As such, the QHY600M PRO camera features advantageous capabilities: a back-illuminated chip with $\geq 87\%$ quantum efficiency, a full well capacity of 51ke^- , and a native 16-bit ADC. Using this camera, we reached a 60 s exposure time.

The other way to have shorter exposure times is to use the binning of the camera pixels. In Table IV, one can see the results of a 2×2 binning. The values, as expected, are around 1/4 of the native pixel values. The trade-off in this latter case is the reduced spatial resolution, as shown in the panels of Fig. 6. Here, depending on

TABLE II. Most important parameters of the medium-resolution setup's configurations at the NORMA facility.

Camera	Lens	Effective pixel size (μm)	Theoretical resolution (μm)	Magnification	Field of view (mm^2)
iKon-M	Milvus 2/100M	26	52	0.5	27×27
Neo 5.5		13	26		33×28
QHY600M PRO		7.5	15		72×48

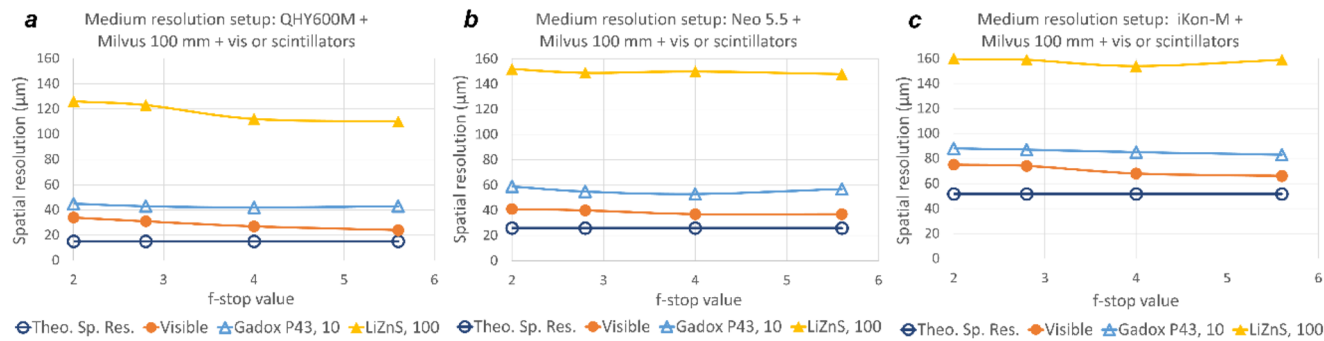


FIG. 5. Calculated (theoretical) and measured spatial resolution values with the various camera configurations for the medium resolution setup at NORMA station [(a) QHY600M PRO, (b) Neo 5.5, and (c) iKon-M].

TABLE III. Comparison of the theoretical and measured spatial resolution values of the medium-resolution setup's configurations at the NORMA facility (see text). Boldface denotes spatial resolution values measured with neutrons using our scintillation screens (Li100 and Gd10).

Camera	Lens	Theo. sp. res. (μm)	Optical sp. res. (μm)	Optical deter. (%)	Li100 sp. res. (μm)	Li100 deter. (μm)	Li100 deter. (%)	Gd10 sp. res. (μm)	Gd10 deter. (μm)	Gd10 deter. (%)
iKon-M		52	60	15	159	99	165	83	23	38
Neo 5.5	Milvus 2/100M	26	37	42	148	111	300	57	20	54
QHY600M PRO		15	24	60	110	86	358	43	19	79

the camera type, the effect of the 3×3 and the 4×4 binning is also shown. Based on the results, we can foresee the frequent use of the 2×2 binning in cases where keeping the spatial resolution has less importance compared to reaching shorter exposure times. It is, however, always mandatory to find a good balance between the parameters to fulfill the actual task's requirements.

The third way to shorten the exposure times while keeping the dynamic range is by collecting more photons from the scintillation events. This ambition led to the construction of a high brightness assembly with infinitely corrected optics, i.e., the high-resolution tandem setup.

B. High-resolution setup

The high-resolution setup has a lower number of configurations; we intend to use it for smaller and/or thinner samples radiographed with higher spatial resolution, and in many cases, we

need to maintain a larger field-of-view (cm's) and appropriate exposure times. Therefore, in all cases, the $10 \mu\text{m}$ thick Gd10 screen mounted on the tandem system was used with cameras with smaller native pixels but a larger chip size. The most important theoretical parameters are tabulated in Table V.

Similarly to the process followed for the medium-resolution configurations, several tests were conducted with both visible light and the Gd-based scintillation screen. During the spatial resolution measurements, the lens aperture was changed in a wide range (from 2 to 5.6), too. It was found that the optical systems in all configurations work with the best spatial resolution toward the higher f-stop values up to 5.6, as shown in the panels of Fig. 7. In Table VI, the tabulated absolute values and percentage changes with an f-stop of 5.6 show how the optical system itself deteriorates the theoretical values. We can conclude that the order in percentage changes is like that of the medium-resolution system, i.e., a bigger relative change for the

TABLE IV. Exposure times in 16-bit or 12-bit depth modes without and with binning (med-res. conf., f-stop = 2).

Camera	Scintillation screen	Bit depth	Exposure time (s) no binning	Exposure time (s) 2×2 binning
iKon-M	Gd10	16	232	63
	Li100	16	12	3
	Gd10	12	38	9
Neo 5.5	Li100	12	2.2	0.54
	Li100	16	30	7
QHY600M PRO	Gd10	16	60	14

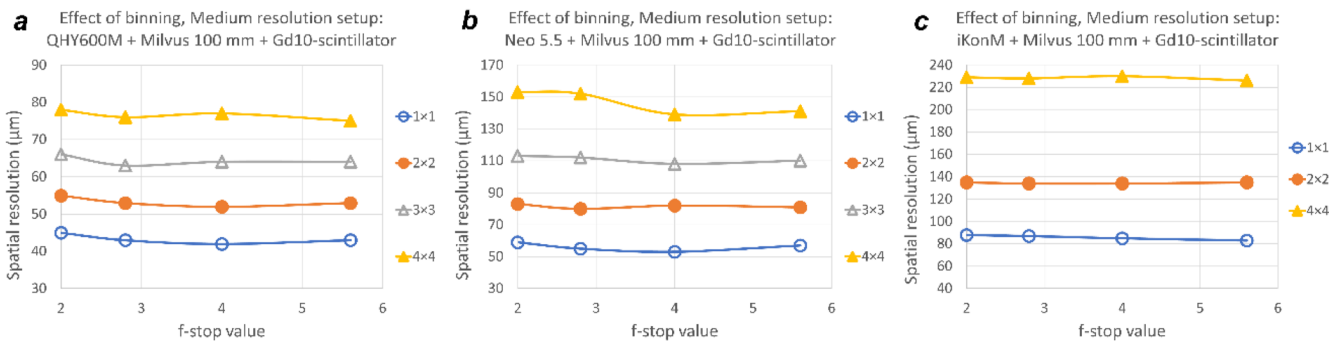


FIG. 6. Spatial resolution values with different binnings for medium-res. configurations [(a) QHY600M, (b) Neo 5.5, and (c) iKonM].

TABLE V. Most important parameters of the high-resolution setup's configurations at the NORMA facility.

Camera	Objective lens	Imaging lens	Effective pixel size (μm)	Theoretical resolution (μm)	Magnification	Field of view ($H \times V$, mm^2)
Neo 5.5	Heliflex 122 mm	Milvus 2/100M	8.1	16.2	0.80	20.8×17.6
QHY600M PRO			4.7	9.4		45×30

configuration with the smaller native pixel size (38% for QHY600M PRO vs 23% for Neo 5.5).

The use of scintillation screens will further reduce optical spatial resolutions. In the panels of Fig. 7, one can see the results of the 2×1 configurations using the two cameras (QHY600M PRO and Neo 5.5) and the Gd-based scintillation screen. Here again, the scintillation screen's inherent blur masks and overrides the pure optical resolution. A detailed comparison is shown in Table VI, where one can follow the degradation effect in the configurations. We found the same effect, i.e., a bigger relative change for the configuration with the smaller native pixel size (177% for QHY600M PRO vs 85% for Neo 5.5).

As examples for exposure time, Table VII shows the measured values in 16-bit and 12-bit depth modes without and with binning, which are significantly lower than in the medium setup, despite the better spatial resolution.

A 2×2 binning, as expected, resulted in exposure times around 1/4 of the native pixel values. The trade-off in this latter case, again, is the reduced spatial resolution, as shown in the panels of Fig. 8. Here, the effect of the 3×3 binning is also shown. An interesting finding is the more elevated degradation effect when applying the 3×3 binning for the Neo 5.5 camera, which can be explained by taking into consideration the two-times larger pixel size compared to that of the QHY600M PRO.

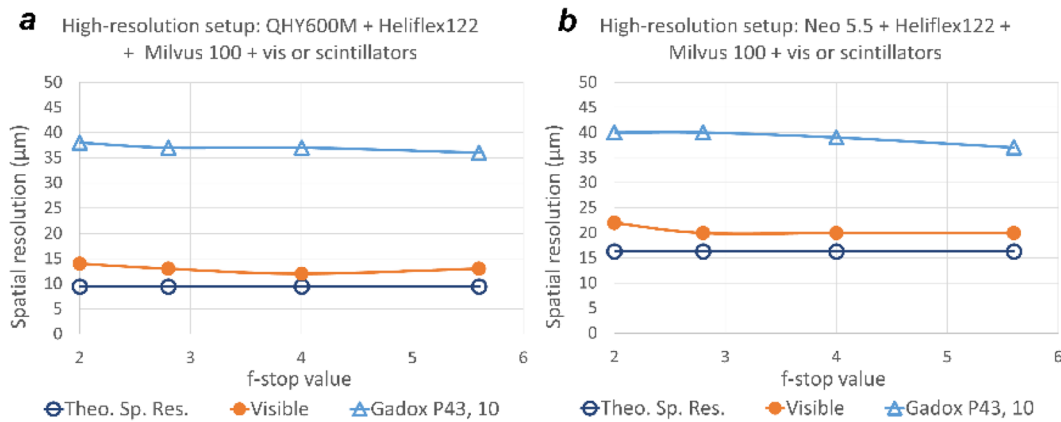


FIG. 7. Calculated and measured spatial resolution values for the high-resolution configurations at NORMA station [(a) QHY600M PRO and (b) Neo 5.5].

TABLE VI. Comparison of the theoretical and measured spatial resolution values of the high-resolution setup's configurations at the NORMA facility (see text). Boldface denotes spatial resolution values measured with neutrons using our scintillation screen (Gd10).

Camera	Lens	Theo. sp. res. (μm)	Optical sp. res. (μm)	Optical deter. (%)	Gd10 sp. res. (μm)	Gd10 deter. (μm)	Gd10 deter. (%)
Neo 5.5	Milvus 2/100M	16.3	20	23	37	17	85
QHY600M PRO		9.4	13	38	36	23	177

TABLE VII. Exposure times in 16-bit and 12-bit depth modes without and with binning (high-res. conf., f-stop = 2, see text).

Camera	Scintillation screen	Bit depth	Exposure time (s) no binning	Exposure time (s) 2×2 binning	Exposure time (s) 3×3 binning
Neo 5.5	Gd10	12	13	3	1.4
QHY600M PRO	Gd10	16	20	5	2

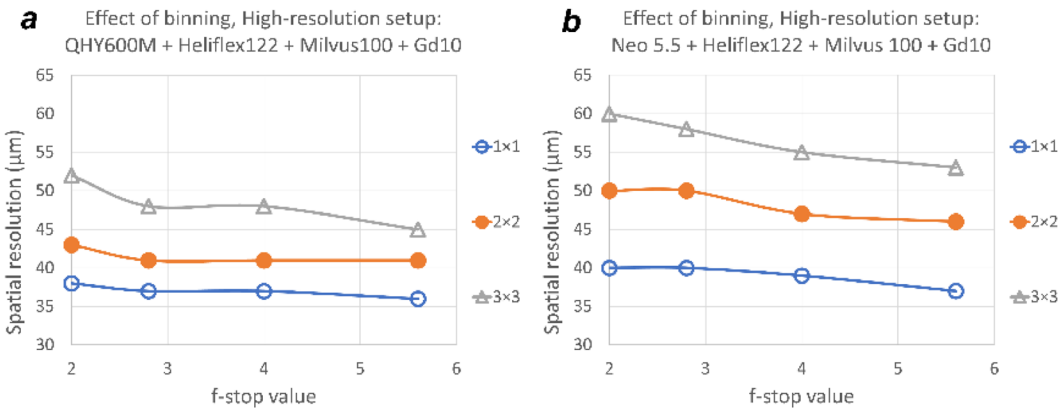


FIG. 8. Spatial resolution values with different binnings for high-resolution configurations [(a) QHY600M PRO and (b) Neo 5.5].

C. Beam divergence and spatial resolution

For an imaging system situated at the end of a neutron guide, knowledge of the real beam divergence is inevitable. The parameter describing its value is the collimation ratio, which is calculable theoretically: $L/D = 1/\tan(2 \times \gamma_c(\lambda))$, where $\gamma_c(\lambda)$ is the energy-dependent total reflection angle for the neutrons in the guide. The calculated L/D is usually less than its measured real value.² Neutrons are reflected from angle zero to the critical angle, and the image is an average result of this angular distribution. Neutrons around the critical angle create only part of the image; smaller angles have a larger influence. Hence, the effective, measured L/D is higher. In addition, the same is true for the whole spectrum of wavelengths, and since the shorter wavelengths in the spectrum are more penetrable than longer wavelengths, they make for better effective L/D . Strictly speaking, one needs to integrate the angular distribution for each wavelength and then over the whole spectrum. The pinhole exchanger at the guide's end made it necessary to apply the real

L/D values because its use will cause dramatically different geometrical blur depending on the distance from the scintillation screen. In practice, using the measured L/D value gives a good enough approximation.

The spatial resolution values were measured using the Gd-stripe at increasing distances from the screen by the iKon-M camera and the LiF-based screen. The values were fitted to derive an estimate that separates detector and penumbra blurring.¹⁴ The L/D value is the slope of the penumbra part of the equation. In Fig. 9, one can clearly see the effect of the primary aperture's size. The largest and smallest apertures result in L/D of 233 and 1832, respectively. In practice, it means that the geometrical blur, e.g., at 80 mm far from the screen, is 6-fold larger for the largest aperture, and it will be added in quadrature to the inherent blur of the screen. In image-driven PGAA measurements, where larger samples regularly appear and can only be positioned at the center of the sample chamber, sharper images help effectively position the volume to be irradiated for elemental analysis. The trade-off is the increased exposure time.

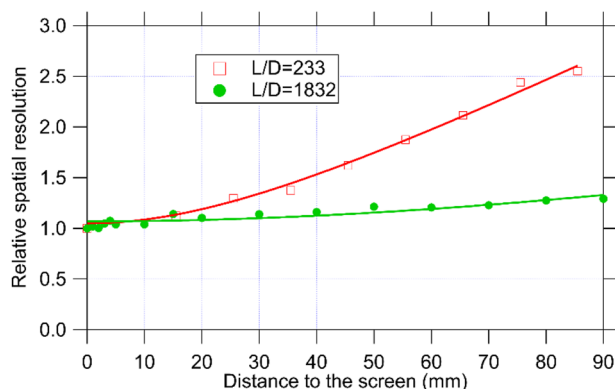


FIG. 9. Change in the relative spatial resolution as a function of both the distance from the screen and the use of the primary apertures (see text).

D. Beam homogenization

For an imaging system using guided neutrons, the intensity distribution in the cross section of the beam is important because an inhomogeneous beam results in poorer neutron statistics in areas

with less flux. At the NORMA facility, the beam intensity is rather inhomogeneous.² A part of this inhomogeneity appears as darker stripes in the images, which are due to the reflections in the guide system built with many separate elements.²⁴ The dark stripes are caused by the gaps at the joints of the guide elements, which are reflected multiple times. The pinhole at the end of the guide forms a pinhole camera that images these stripes onto the detector. The smaller the pinhole, the sharper the image or the projection of the stripes appears. Furthermore, a curved neutron guide has a defined lower cut-off wavelength. One can calculate the beam spread for this cut-off wavelength, and the beam spectrum will be homogeneous only within the cone given by this cut-off wavelength. The full beam will be larger because larger wavelengths have larger critical angles, meaning that the fringes of the beam are caused only by large wavelengths, and the cone outside the one for the cut-off wavelength will be inhomogeneous in wavelengths and spectrum and cause inhomogeneous attenuation for the same material. To mitigate these effects, a movable graphite scatterer was installed at the end of the guide.

In Fig. 10, one can see the effect of the use of the different primary apertures and the graphite scatterers. Without scatterers (upper row in the image), the presence of the stripes increases with smaller apertures, resulting in a more inhomogeneous intensity map. It is, for example, not advantageous during the flat-field

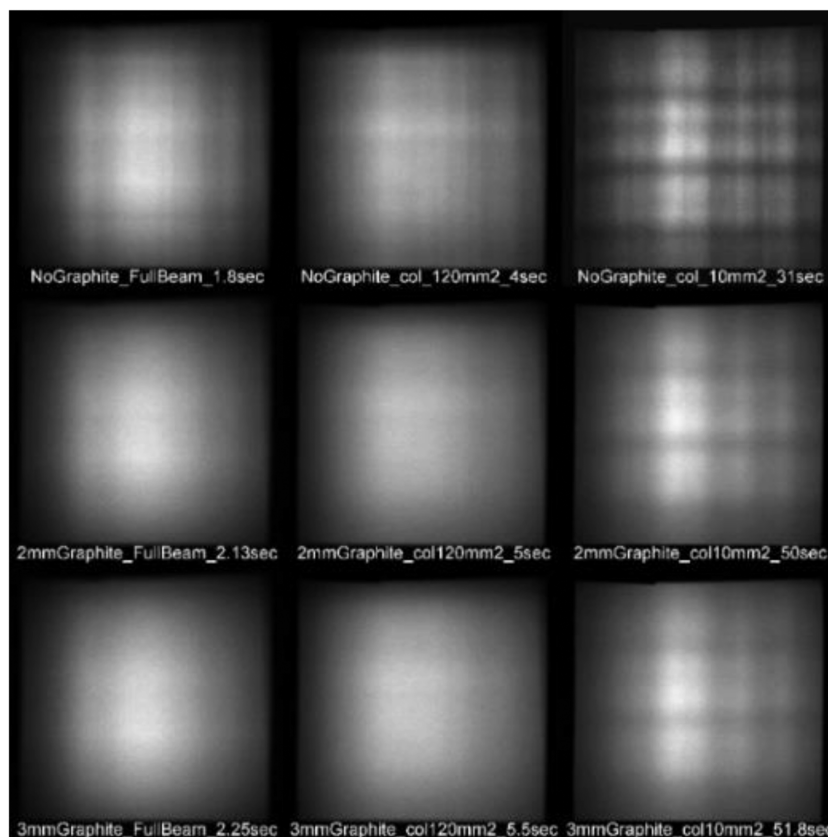


FIG. 10. Change in the beam's intensity map as a function of the use of the primary apertures and graphite scatterers (see text).

correction process. Moreover, the exposure times increase significantly, even to values that are 20-times longer. Applying scatterers (lower rows) will homogenize the intensity maps with the trade-off of slightly increased exposure times (c. 5%–10%).

IV. CONCLUSION AND OUTLOOK

According to the author's intention, this work shows how a neutron imaging system that has worked well for a long time but only partially serves emerging needs can be further developed. The optimal amount of effort and cost can be achieved by changing only those parts of the system that are really needed. In our case, it was not necessary to change the existing and well-functioning hardware and software components that protect the optics and the camera against radiation or handle motor movements and image acquisition. Therefore, we could focus on the optical system chain, from the scintillation screen to the camera. In this chain, the main goal was to make it easily adaptable to different measurement tasks.

The first step was the right choice of scintillation screens with different but complementary light yield and spatial resolution capabilities. Then, the professional macro lens with fixed focus and high brightness allowed its use both in single and tandem configurations with the Heliflex lens. The current tandem setup considerably increases the light collection effectiveness, resulting in a gain factor of 3. Moreover, the use of CCD and sCMOS cameras offers the freedom of choosing the right detector system, too. The range of native pixel and chip sizes provides well-tailored effective pixel size, i.e., spatial resolution and exposure times in the adaptable field of view. For example, according to recent camera developments, one of the available sCMOS type cameras can provide both exceptionally long exposure times and large well depth in small pixels, providing both high dynamic range and good spatial resolution in 16-bit mode.

In summary, it can be said that the newly improved NORMA facility allows the generation of high-quality neutron images, and the planned observations (e.g., higher resolution neutron imaging, local water kinetics in fuel cells) are possible to conduct with this experimental station of the BNC.

ACKNOWLEDGMENTS

This work was part of Project No. RRF-2.3.1-21-2022-00009, titled National Laboratory for Renewable Energy, has been implemented with the support provided by the Recovery and Resilience Facility of the European Union within the framework of Program Széchenyi Plan Plus. The author thanks István G. Szabó and his team at Optika Mérnökiroda Kft., Budapest, Hungary, for both the support during the design process and the manufacturing and installation of the facility. The author thanks László Szentmiklósi, Boglárka Maróti, and Laura Draskovics of the HUN-REN Center for Energy Research for their support.

AUTHOR DECLARATIONS

Conflict of Interest

The author has no conflicts to disclose.

Author Contributions

Zoltán Kis: Conceptualization (lead); Data curation (lead); Formal analysis (lead); Investigation (lead); Methodology (lead); Project administration (equal); Resources (equal); Supervision (lead); Validation (lead); Visualization (lead); Writing – original draft (lead); Writing – review & editing (lead).

DATA AVAILABILITY

The data that support the findings of this study are available from the corresponding author upon reasonable request.

REFERENCES

- ¹T. Belgia, Z. Kis, L. Szentmiklósi, Z. S. Kasztovszky, G. Festa, L. Andreanelli, M. P. De Pascale, A. Pietropaolo, P. Kudejova, R. Schulze, and T. Materna, "A new PGAI-NT setup at the NIPS facility of the Budapest Research Reactor," *J. Radioanal. Nucl. Chem.* **278**(3), 713–718 (2008).
- ²Z. Kis, L. Szentmiklósi, and T. Belgia, "NIPS–NORMA station—A combined facility for neutron-based nondestructive element analysis and imaging at the Budapest Neutron Centre," *Nucl. Instrum. Methods Phys. Res., Sect. A* **779**, 116–123 (2015).
- ³Z. Hózer, I. Nagy, R. Farkas, N. Vér, M. Horváth, T. Novotny, E. Perez-Feró, M. Király, Z. Kis, B. Maróti, L. Szentmiklósi, P. Holecz, G. Auguszt, and G. Gémes, "Experimental simulation of the behavior of E110 claddings under accident conditions using electrically heated bundles," in *Zirconium in the Nuclear Industry: 19th International Symposium* (ASTM International, West Conshohocken, PA, 2021), pp. 813–832.
- ⁴Z. Hózer, I. Nagy, A. Vimi, M. Kunstár, P. Szabó, T. Novotny, E. Perez-Feró, Z. Kis, L. Szentmiklósi, M. Horváth, A. Pintér Csordás, E. Barsy, K. Kulacsy, and M. Grosse, "High-temperature secondary hydriding experiments with E110 and E110G cladding," in *Zirconium in the Nuclear Industry: 18th International Symposium, ASTM STP1597*, edited by R. J. Comstock and A. T. Motta (ASTM International, West Conshohocken, PA, 2018), pp. 1093–1113.
- ⁵T. Rehren, T. Belgia, A. Jambon, G. Káli, Z. Kasztovszky, Z. Kis, I. Kovács, B. Maróti, M. Martinón-Torres, G. Miniaci, V. C. Pigott, M. Radivojević, L. Rosta, L. Szentmiklósi, and Z. Szokefalvi-Nagy, "5,000 years old Egyptian iron beads made from hammered meteoritic iron," *J. Archaeol. Sci.* **40**(12), 4785–4792 (2013).
- ⁶E. Abraham, M. Bessou, A. Ziéglé, M. C. Hervé, L. Szentmiklósi, Z. S. Kasztovszky, Z. Kis, and M. Menu, "Terahertz, X-ray and neutron computed tomography of an Eighteenth Dynasty Egyptian sealed pottery," *Appl. Phys. A* **117**(3), 963–972 (2014).
- ⁷D. Watkinson, M. Rimmer, Z. Kasztovszky, Z. Kis, B. Maróti, and L. Szentmiklósi, "The use of neutron analysis techniques for detecting the concentration and distribution of chloride ions in archaeological iron," *Archaeometry* **56**(5), 841–859 (2014).
- ⁸L. Szentmiklósi, Z. Kis, M. Tanaka, B. Maróti, M. Hoshino, and K. Bajnok, "Revealing hidden features of a Japanese articulated iron lobster via non-destructive local elemental analysis and 3D imaging," *J. Anal. At. Spectrom.* **36**(11), 2439–2443 (2021).
- ⁹B. Maróti, B. Polonkai, V. Szilágyi, Z. Kis, Z. Kasztovszky, L. Szentmiklósi, and B. Székely, "Joint application of structured-light optical scanning, neutron tomography and position-sensitive prompt gamma activation analysis for the non-destructive structural and compositional characterization of fossil echinoids," *NDT&E Int.* **115**, 102295 (2020).
- ¹⁰Z. Kis, F. Sciarretta, and L. Szentmiklósi, "Water uptake experiments of historic construction materials from Venice by neutron imaging and PGAI methods," *Mater. Struct.* **50**(2), 159 (2017).
- ¹¹V. Szilágyi, K. Gméling, Z. Kis, I. Harsányi, and L. Szentmiklósi, "Neutron-based methods for the development of concrete," in *Brittle Matrix Composites 12—Proceedings of the 12th International Symposium on Brittle Matrix Composites, BMC 2019* (Institute of Fundamental Technological Research, Warsaw, Poland (IPPT PAN, 2019), pp. 183–193.

- ¹²L. Szentmiklósi, Z. Kis, B. Maróti, and L. Z. Horváth, "Correction for neutron self-shielding and gamma-ray self-absorption in prompt-gamma activation analysis for large and irregularly shaped samples," *J. Anal. At. Spectrom.* **36**(1), 103–110 (2021).
- ¹³L. Szentmiklósi, B. Maróti, and Z. Kis, "Quantitative, non-destructive elemental composition analysis of 3D-structured samples," *J. Anal. At. Spectrom.* **38**(2), 333 (2022).
- ¹⁴A. P. Kaestner, Z. Kis, M. J. Radebe, D. Mannes, J. Hovind, C. Grünzweig, N. Kardjilov, and E. H. Lehmann, "Samples to determine the resolution of neutron radiography and tomography," *Phys. Procedia* **88**, 258–265 (2017).
- ¹⁵B. Schillinger, W. Chuirazzi, S. Cool, A. Craft, Z. Kis, L. Szentmiklósi, and A. Tengattini, "New measurements on borated neutron imaging screens at Budapest Neutron Centre (BNC)," *J. Phys.: Conf. Ser.* **2605**(1), 012009 (2023).
- ¹⁶J. D. Fairweather, D. Spornjak, A. Z. Weber, D. Harvey, S. Wessel, D. S. Hussey, D. L. Jacobson, K. Artyushkova, R. Mukundan, and R. L. Borup, "Effects of cathode corrosion on through-plane water transport in proton exchange membrane fuel cells," *J. Electrochem. Soc.* **160**(9), F980–F993 (2013).
- ¹⁷J. Kätzel, H. Markötter, T. Arlt, M. Klages, J. Haußmann, M. Messerschmidt, N. Kardjilov, J. Scholta, J. Banhart, and I. Manke, "Effect of ageing of gas diffusion layers on the water distribution in flow field channels of polymer electrolyte membrane fuel cells," *J. Power Sources* **301**, 386–391 (2016).
- ¹⁸Y. Wu, J. I. S. Cho, M. Whiteley, L. Rasha, T. P. Neville, R. Ziesche, R. Xu, R. Owen, N. Kulkarni, J. Hack, M. Maier, N. Kardjilov, H. Markötter, I. Manke, F. R. Wang, P. R. Shearing, and D. J. L. Brett, "Characterization of water management in metal foam flow-field based polymer electrolyte fuel cells using *in-operando* neutron radiography," *Int. J. Hydrogen Energy* **45**(3), 2195–2205 (2020).
- ¹⁹R. F. Ziesche, N. Kardjilov, W. Kockelmann, D. J. L. Brett, and P. R. Shearing, "Neutron imaging of lithium batteries," *Joule* **6**(1), 35–52 (2022).
- ²⁰Y. Zhang, K. R. Chandran, and H. Z. Bilheux, "Imaging of the Li spatial distribution within V_2O_5 cathode in a coin cell by neutron computed tomography," *J. Power Sources* **376**, 125–130 (2018).
- ²¹Z. Kis, T. Belya, and L. Szentmiklósi, "Monte Carlo simulations towards semi-quantitative prompt gamma activation imaging," *Nucl. Instrum. Methods Phys. Res., Sect. A* **638**(1), 143–146 (2011).
- ²²S. H. Williams, A. Hilger, N. Kardjilov, I. Manke, M. Strobl, P. A. Douissard, T. Martin, H. Riesemeier, and J. Banhart, "Detection system for microimaging with neutrons," *J. Instrum.* **7**(2), P02014 (2012).
- ²³A. Tengattini, N. Lenoir, E. Andò, B. Giroud, D. Atkins, J. Beaucour, and G. Viggiani, "NeXT-Grenoble, the Neutron and X-ray tomograph in Grenoble," *Nucl. Instrum. Methods Phys. Res., Sect. A* **968**, 163939 (2020).
- ²⁴N. Kardjilov, A. Hilger, I. Manke, R. Woracek, and J. Banhart, "CONRAD-2: The new neutron imaging instrument at the Helmholtz-Zentrum Berlin," *J. Appl. Crystallogr.* **49**, 195–202 (2016).
- ²⁵N. Kardjilov, M. Dawson, A. Hilger, I. Manke, M. Strobl, D. Penumadu, F. H. Kim, F. Garcia-Moreno, and J. Banhart, "A highly adaptive detector system for high resolution neutron imaging," *Nucl. Instrum. Methods Phys. Res., Sect. A* **651**, 95–99 (2011).
- ²⁶Y. Yehuda-Zada, K. Pritchard, J. B. Ziegler, C. Cooksey, K. Siebein, M. Jackson, C. Hurlbut, Y. Kadmon, Y. Cohen, R. M. Ibberson, C. F. Majkrzak, N. C. Maliszewskyy, I. Orion, and A. Osovitzky, "Optimization of $^6\text{LiF:ZnS(Ag)}$ scintillator light yield using GEANT4," *Nucl. Instrum. Methods Phys. Res., Sect. A* **892**, 59–69 (2018).
- ²⁷T. Neuwirth, B. Walfort, S. Sebold, and M. Schulz, "Light yield response of neutron scintillation screens to sudden flux changes," *J. Imaging* **6**(12), 134 (2020).
- ²⁸W. Chuirazzi, A. Craft, B. Schillinger, S. Cool, and A. Tengattini, "Boron-based neutron scintillator screens for neutron imaging," *J. Imaging* **6**(11), 124 (2020).
- ²⁹B. Tang, W. Yin, Q. Wang, L. Chen, H. Huo, Y. Wu, H. Yang, C. Sun, and S. Zhou, "High quantum efficiency rare-earth-doped $\text{Gd}_2\text{O}_3\text{:S:Tb}$ F scintillators for cold neutron imaging," *Molecules* **28**(4), 1815 (2023).
- ³⁰DXOMark, Zeiss Milvus 2/100M ZF.2 review: Ultra-high performer, <https://www.Dxomark.Com/Zeiss-Milvus-2-100m-Zf-2-Review-Ultra-High-Performer/>, 2016.
- ³¹Digilloyd, Inc., Technical metrics of Zeiss Milvus 100 mm f/2M lens, <https://digilloyd.com/prem/s/ZF/publish/100f2Milvus-metrics.html>, 2016.
- ³²Technical Glass Products, Inc., Trace impurities in fused quartz plates, <https://technicalglass.com/trace-impurities/>, 2024.
- ³³G. Stoeckl, Rodenstock x-ray manual, https://photomacrography.net/archives/heligonlensdocs/00_AllFilesAsZip_Rodenstock_X-ray_lenses_catalogue.zip, 1992, pp. 4.39–4.40.
- ³⁴H. Bien, P. Parikh, and E. Entcheva, "Lenses and effective spatial resolution in macroscopic optical mapping," *Phys. Med. Biol.* **52**(4), 941–960 (2007).
- ³⁵C. Mitja, ImageJ plugin slanted edge MTF, <https://imagej.net/ij/plugins/se-mtf/index.html>, Polytechnic University of Catalonia, 2011.
- ³⁶A. R. Spowart, "Measurement of the absolute scintillation efficiency of granular and glass neutron scintillators," *Nucl. Instrum. Methods* **75**(1), 35–42 (1969).
- ³⁷C. W. E. Van Eijk, A. Bessière, and P. Dorenbos, "Inorganic thermal-neutron scintillators," *Nucl. Instrum. Methods Phys. Res., Sect. A* **529**, 260–267 (2004).